

Cite this: *J. Mater. Chem. A*, 2013, **1**, 3101

## Improved hydrophilicity, permeability, antifouling and mechanical performance of PVDF composite ultrafiltration membranes tailored by oxidized low-dimensional carbon nanomaterials

Jiguo Zhang,<sup>a</sup> Zhiwei Xu,<sup>\*a</sup> Wei Mai,<sup>a</sup> Chunying Min,<sup>b</sup> Baoming Zhou,<sup>a</sup> Mingjing Shan,<sup>a</sup> Yinglin Li,<sup>a</sup> Caiyun Yang,<sup>a</sup> Zhen Wang<sup>a</sup> and Xiaoming Qian<sup>a</sup>

Polyvinylidene fluoride (PVDF)–oxidized carbon nanotubes (OMWCNTs), PVDF–graphene oxide (GO) and PVDF–OMWCNTs–GO composite ultrafiltration membranes were prepared by solution-blending the ternary mixture of PVDF–oxidized low-dimensional carbon nanomaterials–dimethylacetamide in combination with the phase inversion method. The microscope images of the PVDF matrix microstructure showed that the composite membranes exhibited a bigger mean pore size and higher roughness parameters than pristine membranes. The contact angle of the membranes decreased from 78.5° (PVDF) to 66.8° (PVDF–OMWCNTs), 66.4° (PVDF–GO) and 48.5° (PVDF–OMWCNTs–GO). For the PVDF–OMWCNTs, PVDF–GO and PVDF–OMWCNTs–GO composite membranes, there was a 99.33%, 173.03% and 240.03% increase in permeation flux and a 21.71%, 17.23% and 14.29% increase in bovine serum albumin (BSA) rejection, respectively, compared with those of the pristine membranes. The newly developed composite ultrafiltration membranes demonstrate an impressive prospect for the anti-irreversible fouling performance in multi-cycle operations from BSA treatment. Additionally, the addition of OMWCNTs and GO increased the tensile strength of composite membranes from 1.866 MPa to 2.106 MPa and 2.686 MPa, respectively. Conspicuously, the PVDF composite ultrafiltration membranes endowed with oxidized low-dimensional carbon nanomaterials demonstrated fascinating hydrophilicity, permeability, antifouling and mechanical performance and promising application prospects owing to the rich oxygen-containing functional groups, high specific surface and synergistic effect of inorganic additive.

Received 8th September 2012  
Accepted 2nd January 2013

DOI: 10.1039/c2ta01415g

[www.rsc.org/MaterialsA](http://www.rsc.org/MaterialsA)

### Introduction

Ultrafiltration has been used extensively in many membrane separation and filtration processes, especially in wastewater treatment, and chemical and biochemical fields, such as oil-water separation and protein effluent separation.<sup>1–6</sup> The hydrophilicity and porous structure of membranes are important factors to consider in the membrane manufacturing processes.<sup>7</sup> A good porous membrane used in these processes must have high permeability, good hydrophilicity and excellent chemical resistance to the feed streams. Poly(vinylidene fluoride) (PVDF) is a common ultrafiltration, microfiltration and pervaporation membrane material because of its excellent chemical resistance and thermal stability.<sup>8–10</sup> Recently, modification of PVDF membranes has been extensively investigated to

improve the membrane hydrophilicity and permeation. The chemical modification method could be employed to improve the hydrophilicity of the membrane, but the main chain of the PVDF molecule would be changed and the advantages of the PVDF membrane might be decreased.<sup>11</sup> Additionally, besides the amphiphilic copolymers, inorganic particles such as Al<sub>2</sub>O<sub>3</sub>, SiO<sub>2</sub>, TiO<sub>2</sub>, ZrO<sub>2</sub>, Fe<sub>3</sub>O<sub>4</sub>, LiOCl<sub>4</sub> and CdS were also introduced in the PVDF solutions in fabricating organic–inorganic hybrid membranes.<sup>12–21</sup> It has also been demonstrated that the addition of inorganic fillers has led to an increase in the membrane hydrophilicity, pure water flux, rejection, antifouling mechanical strength and effective control of the membrane surface performance.<sup>12,14–18</sup> But there are no oxygen-containing functional groups on the surface of the inorganic materials mainly used in previous studies, resulting in the fact that the hydrophilicity and permeability cannot be increased satisfactorily. In addition, the low specific surface area reduced the adhesion strength at matrix/filler interfaces, which may make the mechanical performance unsatisfactory. As a result, the oxygen-containing functional groups and high specific surface area of

<sup>a</sup>State Key Laboratory of Hollow Fiber Membrane Materials and Processes, School of Textiles, Tianjin Polytechnic University, Tianjin 300387, People's Republic of China. E-mail: xuzhiwei@tjpu.edu.cn; Fax: +86 022 83955231; Tel: +86 022 83955231

<sup>b</sup>School of Material Science and Engineering, Jiangsu University, Zhenjiang 212013, China

oxidized low-dimensional nanomaterials are expected to endow the membrane with enhanced hydrophilicity, pure water flux, rejection, antifouling and mechanical performance under low concentration.

One-dimensional carbon nanotubes and two-dimensional graphene possess remarkable chemical, mechanical and physical properties, such as extremely high aspect ratio, easy functionalization of the surface and a unique graphitized plane structure,<sup>22–26</sup> which are important factors in enhancing the contact area with the polymer. As a result, these materials show promise for application as nanofiller materials in polymer composite membranes. To date, several authors have shown the successful preparation of carbon nanotube (MWCNTs) blended polymeric membranes<sup>27–36</sup> and they have studied mainly the effects of MWCNTs or the functionalized MWCNTs on the performance of membranes. However, a comparative study of different architectures of the one-dimensional oxidized carbon nanotubes (OMWCNTs) and two-dimensional GO in the performance modification of composite ultrafiltration membranes has not been reported. In addition, the effects of GO and the synergistic effect of OMWCNTs and GO on the microstructure and performance of composite ultrafiltration membranes have not been investigated in detail.

Based on these considerations and the body of previous research, the objective of this work was to synthesize OMWCNTs or graphene oxide (GO)-PVDF composite membranes using the non-solvent induced phase separation method,<sup>37</sup> determine their hydrophilicity, pure water flux, rejection, antifouling and mechanical strength and explore the role of oxygen-containing groups and architecture of oxidized low-dimensional carbon nanomaterials in composite membrane performance. The morphology of all the samples was characterized using a scanning electron microscope (SEM) and atomic force microscope (AFM). The mechanical performance was determined by using a tensile tester. Water contact angle (CA), water flux, bovine serum albumin (BSA) rejection and antifouling measurements were also carried out for membrane hydrophilicity and permeability.

## Experimental

### Materials

The PVDF (FR904) was purchased from Shanghai 3F New Materials Co. Ltd. China. *N,N*-dimethylacetamide (DMAc, >99.5%, reagent) and polyvinyl pyrrolidone (PVP) were purchased from Tianjin Weichen Chemical Reagent Co. Ltd. China. Multi-walled carbon nanotubes (MWCNTs, with diameters of 10–50 nm and length of 1–30  $\mu\text{m}$ ) were obtained from Nanjing XF Nanomaterial Science and Technology Co. Ltd. The purity of received MWCNTs was 95%. Graphene oxide was prepared by an improved Hummers' method.<sup>38</sup> Distilled water was used as the nonsolvent for polymer precipitation.

### Preparation of OMWCNTs

In order to remove the impurities of raw carbon nanotubes (such as the metallic catalyst particles and amorphous carbon)

and increase functional groups on the surface of MWCNTs, 2 g of raw carbon nanotube was soaked in 160 ml solution of  $\text{HNO}_3\text{-H}_2\text{SO}_4(1/3, v/v)$  and heated to 70  $^\circ\text{C}$  for 8 h without stirring.<sup>39</sup> The solution was diluted with 2 l pure water and filtered through a 0.45  $\mu\text{m}$  membrane. The OMWCNTs were washed with pure water to reach neutral pH and dried at 55  $^\circ\text{C}$  in a vacuum for 8 h.

### Preparation of the membranes

A variety of composite PVDF membranes were prepared by the phase inversion process method. For the PVDF-OMWCNTs composite membranes, the OMWCNTs with a concentration of 1 wt% (mass of OMWCNTs/mass of polymer) were dispersed in 84 g DMAc by an ultrasonicator for at least 2 h, which facilitated the dispersion of OMWCNTs, then, 15 g PVDF was completely dissolved in the OMWCNTs solution at 40  $^\circ\text{C}$ , and simultaneously another additive (1 g PVP) was dissolved in the solution. For the membranes of PVDF-GO, the concentration of GO was the same as that of OMWCNTs in the casting solutions. For the PVDF-OMWCNTs-GO membranes, the given amount of OMWCNTs and GO (1/9, g/g) were separately dispersed in DMAc by an ultrasonicator for at least 2 h first, and then the PVDF was added to the OMWCNT-GO solution. In order to identify all three composite membranes easily, the above membranes were named as P-OMW, P-GO and P-OMW-GO, correspondingly. For the composite membranes, the low concentration (1 wt%) of inorganic particles was selected to compare the oxidized low-dimensional carbon nanomaterials with other particles. For the P-OMW-GO, the weight ratio (1/9) of MWCNTs and GO was adopted according to the literature,<sup>40</sup> which indicated that the stacking of individual two-dimensional GO could be effectively inhibited by introducing one-dimensional OMWCNTs. Among all the steps, in order to obtain optimal dispersions of the OMWCNTs and GO in the polymer solutions, agitation was required for at least 24 h at 40  $^\circ\text{C}$ .

The casting solution of pure PVDF membranes was prepared by dissolving 15 g PVDF and 1 g PVP in 84 g DMAc. After releasing the bubbles in a vacuum oven, the casting solution was cast on a glass plate at 1.2  $\text{m min}^{-1}$  and 40  $^\circ\text{C}$  with a casting knife of 200  $\mu\text{m}$  space. Then, the membranes were immediately immersed in a tap water coagulation bath at room temperature. The formed membranes were peeled off and subsequently washed with distilled water to remove residual solvent. Several pieces of each kind of membrane were kept at room temperature for SEM/AFM and water CA measurements. To prepare the samples for the mechanical property tests, the wet membranes were directly dried in the air at room temperature. The residual membranes were kept in distilled water for the filtration tests.

### Characterization of low-dimensional carbon nanomaterials

Transmission electron microscopy (TEM) observation of MWCNTs and OMWCNTs was performed using a Hitachi 7650 operated at 200 kV. The surface morphology of GO was examined using AFM (CSPM5500) and the samples were dispersed by sonication in a mixture of pure water, then dried and the AFM tested under the non-contact mode. Fourier-Transform Infrared

spectroscopy (FTIR) was used to identify functional groups on the surface of OMWCNTs and GO.

### Characterization of membranes

**SEM, AFM characterization, overall porosity, mean pore size calculation and pore-diameter distributions.** Membrane microstructures, the top surface, as well as the cross-section, were observed under a field emission SEM (Quanta 200, Holland). The cross-sections were prepared by fracturing the membranes at the temperature of liquid nitrogen. All specimens were coated with a thin layer of gold before being observed using SEM. The membrane surface morphology, in terms of the mean surface roughness ( $R_a$ ), root mean square ( $R_q$ ) and mean difference in the height between the five highest peaks and the five lowest valleys ( $R_z$ ) was studied by AFM (CSPM5500). The method was studied by AFM under the non-contact mode. In the range of the scan areas  $10\ \mu\text{m} \times 10\ \mu\text{m}$ , roughness parameters could also be obtained with the AFM analysis software, small squares of the prepared membranes (approximately  $1\ \text{cm}^2$ ) were cut and glued on the glass substrate before being scanned ( $10\ \mu\text{m} \times 10\ \mu\text{m}$ ).

The overall porosity ( $\varepsilon$ ) was determined by the gravimetric method,<sup>41</sup> as defined in the following equation:

$$\varepsilon = \frac{\omega_1 - \omega_2}{A \times l \times d_w} \times 100\% \quad (1)$$

where  $\omega_1$  is the weight of the wet membrane,  $\omega_2$  is the weight of the dry membrane,  $A$  is the membrane effective area ( $\text{m}^2$ ),  $d_w$  is the water density ( $0.998\ \text{g cm}^{-3}$ ) and  $l$  is the membrane thickness (m). The Guerout–Elford–Ferry equation (eqn (2)) was utilized to determine the membrane mean pore radius ( $r_m$ ) on the basis of the pure water flux and porosity data:<sup>42</sup>

$$r_m = \sqrt{\frac{(2.9 - 1.75\varepsilon) \times 8\eta l Q}{\varepsilon \times A \times \Delta P}} \quad (2)$$

where  $\eta$  is the water viscosity ( $8.9 \times 10^{-4}\ \text{Pa s}$ ),  $Q$  is the volume of the permeate pure water per unit time ( $\text{m}^3\ \text{s}^{-1}$ ) and  $\Delta P$  is the operation pressure (0.1 MPa).

The pore-diameter distributions were obtained by capillary flow porometry measurements.<sup>43</sup> The membrane sample was wetted by immersing it in ethanol for 24 h at room temperature, which was found to be sufficient for obtaining consistent data. The wet membrane sample was mounted in the sample holder after dripping out excess ethanol clinging onto the membrane surface. First, a wet run was performed using a solvent filled sample that was followed by a dry run (sample without wetting liquid) for obtaining flow rate curves as a function of applied pressure. This procedure was adopted to avoid subjecting the membrane to a high gas flow during the dry run that may distort the physical structure of pores. The measured ratio ( $\varphi$ ) of flow rates through the wet ( $F_w$ ) and dry sample ( $F_d$ ) can be used for obtaining the flow-based pore-diameter distribution  $f_F(D)$  as:

$$\varphi = \frac{F_w}{F_d} = \int_{D_{\min}}^{\infty} f_F(D) dD \quad (3)$$

where  $D_{\min}$  is the diameter of the smallest constriction of pores that have been opened by maximum applied pressure.

**Water CA measurements.** The CA between water and the membrane surfaces was measured with contact-angle measurement apparatus (JYSP-180 Contact Angle Analyzer) based on the sessile-drop method. Briefly, a water droplet was deposited on a flat homogeneous membrane surface and the contact angle of the droplet with the surface was measured. The instantaneous CA obtained within 0.2 s (ensuring observable vibration of the liquid drop on the solid sample had already ceased) was recorded. Each final CA value was obtained by averaging over more than five CA values of different spots.

**The permeation flux and rejection measurements.** Permeation flux and rejection of the membranes were measured by ultrafiltration (UF) experimental equipment. The rejection tests were carried out with an aqueous solution of BSA (molecular weight = 67 000) ( $1\ \text{g l}^{-1}$ ). All experiments were conducted at 25 °C and under the feed pressure of 0.1 MPa. The measuring protocol was depicted as follows: for the first 30 min, the membrane was compacted at 0.1 MPa to get a steady flux; then the flux was recorded at 0.1 MPa every 5 min, and at least 5 readings were collected to obtain an average value. After this, pure water was changed to  $0.1\ \text{g l}^{-1}$  BSA solution. The concentrations of BSA in the permeation and feed solution were measured by an UV-spectrophotometer (Shimadzu UV-2450, Japan). The permeation flux and rejection were defined using the following eqn (4) and (5), respectively:

$$J = \frac{Q}{A \times T} \quad (4)$$

$$R = \left(1 - \frac{C_P}{C_F}\right) \times 100\% \quad (5)$$

where  $J$  is the permeation flux of the membrane for pure water ( $\text{l m}^{-2}\ \text{h}^{-1}$ ),  $Q$  is the volume of permeate pure water (l),  $A$  is the effective area of the membrane ( $\text{m}^2$ ) and  $T$  is the permeation time (h).  $R$  is the rejection to BSA (%),  $C_P$  and  $C_F$  are the concentrations of BSA in the permeation and feed solution, respectively (wt %).

**Fouling and physical cleaning.** For the fouling resistance test, pure water was first passed through the membrane until the flux remained stable over at least half an hour. After testing the pure water flux, the cell was then emptied and refilled with the model protein solutions comprised of  $1\ \text{g l}^{-1}$  BSA in PBS with a pH of 7.4, the fouling experiments were then carried out. After BSA ultrafiltration, the fouled unit and membrane were cross-flow cleaned with pure water for 20 min and then refilled with pure water as a feed to determine the reversibility of fouling. All cycles were performed three times. In order to evaluate the fouling-resistant ability of the blended membranes, the flux recovery ratio (FRR) was used. FRR was calculated using the following expression:

$$\text{FRR} = \frac{J_{W2}}{J_{W1}} \times 100\% \quad (6)$$

where  $J_{W1}$  and  $J_{W2}$  are the pure water flux of clean and fouled membrane after being cleaned, respectively.

To analyze the fouling process in detail, several equations were used to describe the fouling resistance of the membranes.<sup>44</sup>

The resistance formed during the filtration process can signify the fouling of the membrane. The total fouling ratio ( $R_t$ ), reversible fouling ratio ( $R_r$ ) and irreversible fouling ratio ( $R_{ir}$ ) were defined and calculated as follows:

$$R_t = \left(1 - \frac{J_p}{J_{w1}}\right) \times 100\% \quad (7)$$

$$R_r = \left(\frac{J_{w2} - J_p}{J_{w1}}\right) \times 100\% \quad (8)$$

$$R_{ir} = \left(\frac{J_{w1} - J_{w2}}{J_{w1}}\right) \times 100\% \quad (9)$$

Obviously,  $R_t$  is the sum of  $R_r$  and  $R_{ir}$ .

**Mechanical strength tests.** The membrane strength was measured by testing the tensile strength and elongation-at-break of membrane coupons (2 cm × 15 mm) with a YG028 tensile tester (Wenzhou fangyuan instrument Co. Ltd., China). All the tensile tests were carried out at a stepper motor speed of 10 mm min<sup>-1</sup> at room temperature and the thickness of the sample was measured according to the vernier caliper. Results were averaged from five samples.

## Results and discussion

### Morphology and functional group characterization of OMWCNTs and GO

TEM and AFM were utilized to characterize the surface morphology of the OMWCNTs and GO. Fig. 1(a) and (b) show that the raw MWCNTs were shortened to the lengths of 0.2 μm–1.0 μm with a strong acid mixture treatment. This will play a positive role for improving the dispersibility of OMWCNTs with PVDF matrix. In Fig. 1(c), the thicknesses of pristine GO single-

layer sheets we prepared were mostly within a range of 1.2–1.5 nm, which is a little bigger than that reported due to the extensive oxidation during the preparation process. From Fig. 1(d), we can see that the suspensions produced by the sonication of graphite oxide are confirmed to consist mainly of single-layer GO platelets.

FTIR is a powerful tool in investigating functional groups of the OMWCNTs and GO. The new peaks emerging at 1680 and 3300–3600 after the acid treatment correspond to carboxyl groups and hydroxyl groups, respectively (Fig. 2). This confirms the attachment of the functional groups onto the MWCNTs. There are also carboxyl groups and hydroxyl groups on the surface of GO, which would be beneficial in evidencing the improvement of the membrane hydrophilicity. These results are in good agreement with the results of previous reports.<sup>45</sup> Meanwhile, the hydrophilic properties of these functional groups improve the dispersibility of OMWCNTs and GO in aqueous solution.

### Membrane morphology

In order to investigate the effect of OMWCNTs and GO on the microstructure of the membranes, SEM micrographs and AFM analyses of PVDF membranes with different compositions have been obtained. Fig. 3 shows the SEM pictures of the top and cross-section (from left to right) views of the membranes. As depicted in Fig. 3, the top surface has a denser nodular-like structure caused by the delayed demixing during the phase inversion process. The mechanism of the formation of this structure has been discussed in a previous report.<sup>46</sup> We can also visibly find the OMWCNTs from the surface of membranes through SEM (B-a in Fig. 3), which indicates that the membranes are well tailored by nanomaterials. As to the cross-sectional structure, all the membranes exhibit the typical asymmetric structure, consisting of a skin layer as a selective barrier and a much thicker fingerlike sub-structure. This structure was mainly due to the high mutual diffusivity of water and DMAc.<sup>47</sup> Additionally, it can be seen that with oxidized carbon nanomaterials tailored, a typical transition from an asymmetric structure to a microcellular structure could be observed, and the topical asymmetric structure of the

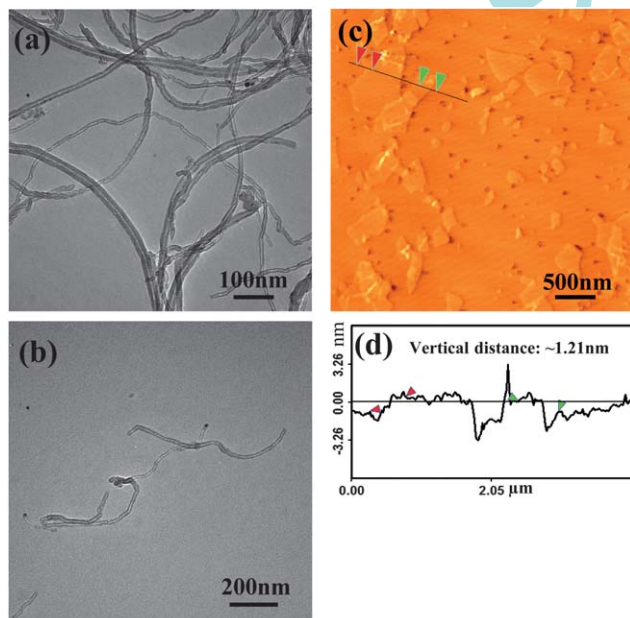


**Fig. 1** TEM images of (a) MWCNTs, (b) OMWCNTs, (c and d) tapping mode AFM topographic images and height profiles of GO dispersed in water.

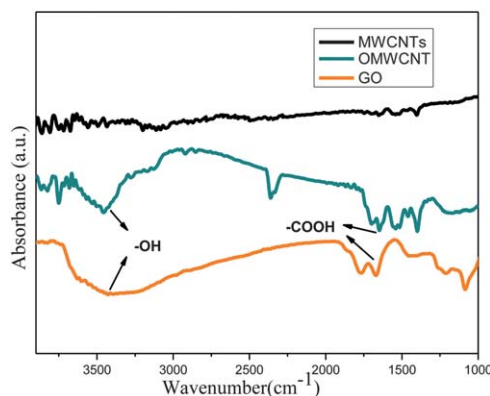


**Fig. 2** FTIR spectra of MWCNTs, OMWCNTs and GO.

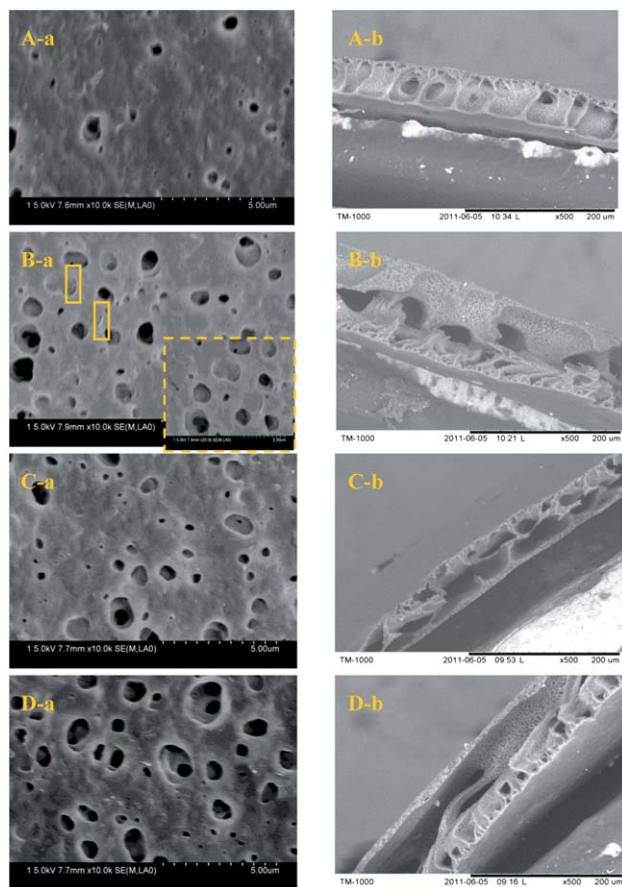


**Fig. 3** The (a) top and (b) cross-section views of (A) PVDF; (B) P-OMW; (C) P-GO and (D) P-OMW-GO.

membrane cross-section became faint and the structure of the sublayer underwent a transition from finger-like (PVDF) to a sponge-like structure (P-OMW, P-GO and P-OMW-GO). This result may be explained by the fast exchange of solvent and non-solvent in the phase inversion process due to the hydrophilic nanomaterials<sup>48</sup> and occurring interactions between components in the casting solution and phase inversion kinetics.<sup>49</sup>

Fig. 4 shows the three-dimensional surface AFM images of the composite PVDF membrane surfaces. The roughness parameters of the surfaces of the PVDF/composite membranes are given in Table 1. Roughness parameters could be obtained with the AFM analysis software. There exists mean roughness ( $R_a$ ), root mean square of Z data ( $R_q$ ) and mean difference in the height between the five highest peaks and the five lowest valleys ( $R_z$ ). It was observed that all the roughness parameters of the modified membranes were larger than those of the pure PVDF membrane (showed in Table 1). The roughness of P-OMW, P-GO and P-OMW-GO composite membranes was 62.09%, 89.56% and 95.05% higher than that of the PVDF alone. From the Wenzel model,<sup>50</sup> we can see that as hydrophilic materials, the large surface roughness will achieve a low contact angle. Additionally, due to the stacking of individual two-dimensional GO being effectively inhibited by introducing one-dimensional OMWCNTs,<sup>40</sup> the P-OMW-GO has the biggest roughness, which

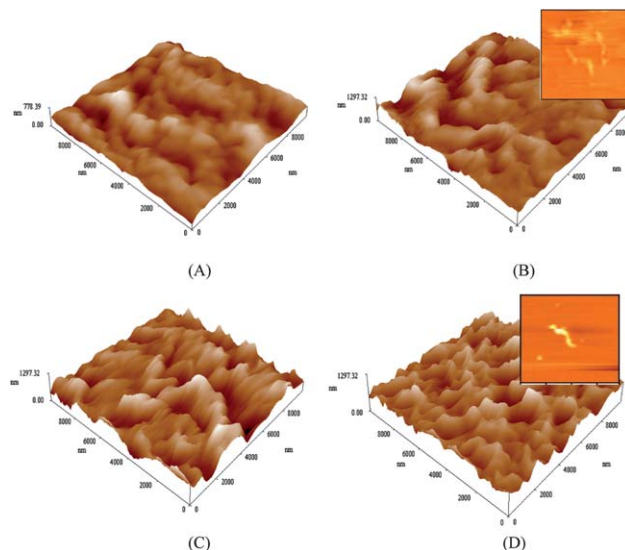


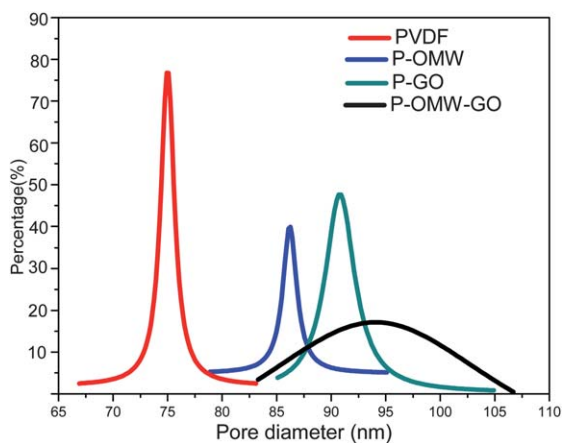
**Fig. 4** AFM three-dimensional surface images of membranes: (A) PVDF; (B) P-OMW; (C) P-GO and (D) P-OMW-GO (the OMWCNTs are magnified in the two-dimensional AFM images).

is beneficial to the hydrophilicity. It is well known that the membrane with high surface roughness increases surface area and causes cavities, both promoting permeation.<sup>18</sup> This was the reason that the membranes permeation trend increased with roughness owing to contaminants accumulating in the valleys of the rough membrane surface. These results show that increased membrane-surface roughness does not have a negative effect on membrane performance, rather, it effectively improves the permeating flux (details in a later part).

The overall porosity information of the membranes is presented in Table 1. The results of the porosity measurement revealed that all the modified membranes possessed a good porosity in the range of 78–82%, while the raw membrane had a porosity of 69.58%. This can be explained as follows. By mixing hydrophilic nanomaterials with the matrix of PVDF polymer, due to fast exchange of the solvent and non-solvent in the phase inversion process, the overall porosity of the prepared membranes was improved.<sup>51</sup> Furthermore, increased mean pore size was obtained for composite membranes (Table 1), which could be calculated on the basis of the pure water flux and porosity data. The formation of pores could be interpreted as follows. The carboxyl groups have a good affinity to water. The addition of the oxidized low-dimensional carbon nanomaterials increases the solution thermodynamic instability in the gelation bath (nonsolvent), which promotes a rapid phase demixing, resulting in large pore formation in low amounts of the nanomaterials at the membrane skin layer.<sup>52</sup> Accordingly, the composite membranes were all endowed with an advantageous porous surface, which undoubtedly plays a positive role in promoting membrane permeability.<sup>7,53</sup> Pore-diameter distributions were also an important factor for the performance of membranes. From Fig. 5, it is clear that the pore-diameter distributions of P-GO and P-OMW-GO were uneven, especially for P-OMW-GO. This may have the adverse effect on rejection

**Table 1** Porosity, surface mean pore size and roughness parameters for membranes PVDF, P-OMW, P-GO and P-OMW-GO

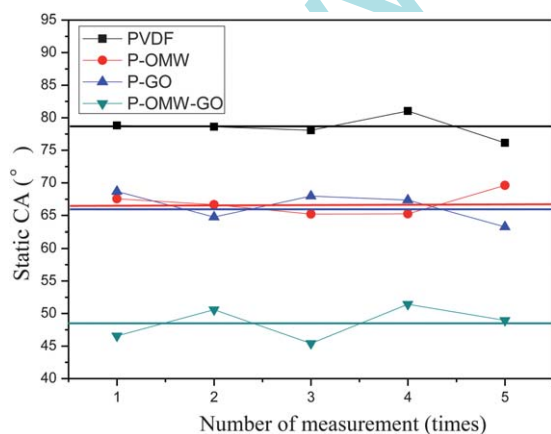
Membranes	Porosity (%)	Average diameter (nm)	Surface area ( $\mu\text{m}^2$ )	Roughness		
				$R_a$ (nm)	$R_q$ (nm)	$R_z$ (nm)
PVDF	69.58	74.83	104.98	72.2	93.5	656
P-OMW	78.14	85.56	128.34	118	153	1200
P-GO	79.59	90.63	136.16	138	180	1270
P-OMW-GO	82.09	94.04	142.91	142	182	1300

**Fig. 5** The pore-diameter distributions of different membranes.

and mechanical performance to some extent, which is discussed in a later part.

### Hydrophilicity of the membranes

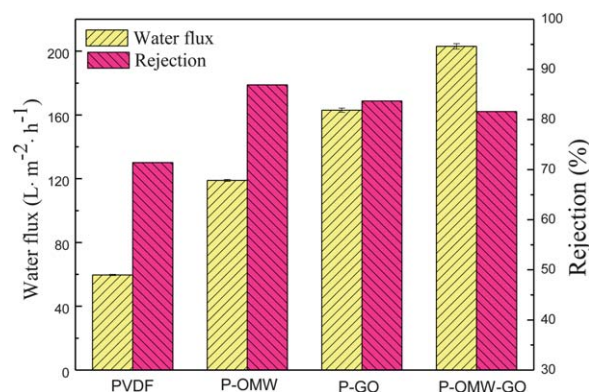
The water CA is an important parameter for measuring surface hydrophilicity.<sup>54</sup> In general, a smaller CA corresponds to a more hydrophilic material. The CA measured immediately after water was dropped onto the membrane surface would preferably reflect the natural wettability of the material. The CA results are shown in Fig. 6, from which an obvious trend could be drawn

**Fig. 6** Static CA of membranes with different oxidized low-dimensional carbon nanomaterials measured five times (the straight lines indicate the mean value of CA for each sample).

that the CA values decreased (hydrophilicity increased) when OMWCNTs and GO were added. From the linear graph, it seems that all the points met the trend. These results demonstrated that adding oxidized carbon nanomaterials to PVDF could improve its hydrophilicity, which is based on that hydrophilic oxygen-containing functional groups migrated spontaneously to the membrane surface to reduce the interface energy during the phase inversion process, making the membrane surface hydrophilic.<sup>55</sup> This might play a favourable role in elevating the water flux of the composite membranes.<sup>4</sup> For another, a margin of error of the hydrophilicity of P-OMW and P-GO composite membranes shows that the oxygen-containing functional groups are all playing their role efficiently. We can also find that P-OMW-GO even achieved  $48.582^\circ$ , which is the lowest among all membranes. The results reveal a synergistic interaction between the GO and OMWCNTs based on GO protection against aggregation of the OMWCNTs and the long OMWCNTs can construct a hierarchical OMWCNTs-GO architecture to inhibit the accumulation of GO,<sup>56</sup> which makes the oxygen-containing functional groups more efficient. Additionally, it has been demonstrated that nanometer size surface roughness strongly influences the hydrophilic behavior of water at the surface of membranes,<sup>57</sup> which was discussed in an earlier part, and the synergistic enhancement of hydrophilicity for the membranes is coordinated with the surface roughness.

### Permeation flux and rejection

Fig. 7 shows the pure water flux about the pure PVDF membrane and composite membranes. Here, the pure water flux of the

**Fig. 7** Comparison of pure water flux and BSA rejection of the membranes PVDF, P-OMW, P-GO and P-OMW-GO.

composite membranes showed a similar trend to the hydrophilicity trend of the composite membranes. This is due to the fact that the oxidized low-dimensional carbon nanomaterials–PVDF membranes were successfully endowed with the vital performance of permeation. It is also known that the improved hydrophilicity of the membranes can enhance the water permeability by attracting water molecules inside the membrane matrix and facilitating them to pass through the membrane.<sup>58</sup> Moreover, water permeation is determined by the pore size of the entire membrane and the advantageous porous surface. Judging from Table 1, the overall morphological characteristics seem to be similar. For the P-OMW and P-GO, the slight improvement in permeation for P-OMW compared with P-GO can be ascribed to the higher specific surface and more oxygen-containing functional groups of GO. It is interesting to note that the pure flux of P-OMW–GO increases from  $59.7 \text{ l m}^{-2} \text{ h}^{-1}$  to  $203 \text{ l m}^{-2} \text{ h}^{-1}$  and outperforms that of P-OMW and P-GO, which indicates the synergetic effect of OMWCNTs and GO for the permeation of composite membranes. The synergetic enhancement of P-OMW–GO can be explained by the inhibited aggregation of OMWCNTs and GO,<sup>40</sup> which results in an increase of hydrophilicity and pore size of P-OMW–GO owing to the satisfactory exposed surface of nanomaterials, compared with those of P-OMW and P-GO.

The BSA rejection results of different membranes are shown in Fig. 7. Compared with that of pure PVDF membranes (71.4%), the BSA rejection of P-OMW, P-GO and P-OMW–GO was enhanced by 21.71%, 17.23% and 14.29%, respectively. The significant effect of oxidized low-dimensional carbon nanomaterials on promoting membrane rejection might be related to the complete absorptive action.<sup>59</sup> All of the composite membranes had dense outer surfaces, as shown in Fig. 3, which contacted with BSA solutions and could determine the extent of BSA rejection mainly.<sup>60</sup> There was a slight decrease in BSA rejection for P-GO (83.7%) with the larger pore size compared with that for P-OMW (86.9%) (Table 1), because BSA molecules have more opportunity to penetrate through larger membrane pores.<sup>7,61</sup> Additionally, the BSA rejection of P-OMW–GO was slightly lower than that of P-OMW and P-GO, though P-OMW–GO has the best hydrophilicity, which is answered by the pore size increase and nonuniform size distribution shown in Fig. 5.

### Anti-irreversible fouling performance in multi-cycle operations

To determine the effect of oxidized low-dimensional carbon nanomaterials on fouling resistance, the cyclic filtration tests were performed on the pure PVDF membrane and modified PVDF membranes. The results of these filtration runs are shown in Fig. 8. The operated ultrafiltration process can be divided into three phases. The first half hour in the curve is referred to pure water ultrafiltration. The second phase is 1 h ultrafiltration of BSA in PBS solution. The third phase is a simple membrane cleaning by pure water flushing and then the pure water flux is measured again for another half an hour. The permeation flux of the BSA in PBS solution decreased rapidly compared to the flux of pure water at the initial stage because of protein fouling

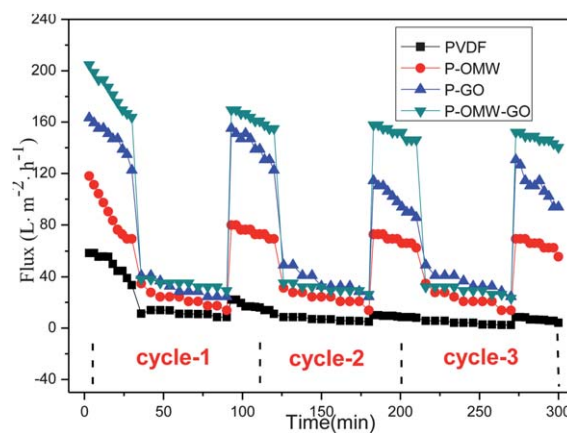


Fig. 8 Time-dependent flux of different membranes with three cycles of BSA solution ultrafiltration.

and concentration polarization. The effects of concentration polarization can be effectively reduced using high speed stirring of the protein solution at 300 rpm.<sup>62</sup> Therefore, the decrease in the permeation is mainly coming from the protein fouling in this experiment. Because the protein molecules may be entrapped in the pores and block the channels, which cannot be removed by hydraulic cleaning for membranes, the water flux of all the membranes after cleaning cannot completely resume at the initial value. Nevertheless, it is clear that all of the modified membranes keep a slight decrease compared with the initial flux throughout the three filtration cycles in Fig. 8, whilst the initial flux of the unmodified PVDF continued decreasing. This suggested that the permeability of pure PVDF was significantly influenced by physically irreversible fouling and could not recover as well as the modified membranes. Although there are only a few works in which membrane fouling is directly correlated to the hydrophilicity of the membrane surface,<sup>63</sup> it is generally assumed that an increase in hydrophilicity on membrane surfaces increases the fouling resistance, since proteins such as BSA are hydrophobic in nature.<sup>64</sup> To monitor the irreversible membrane fouling, the pure water flux ( $J_{w2}$ ) is measured after membranes are cleaned. Fig. 9 shows the flux

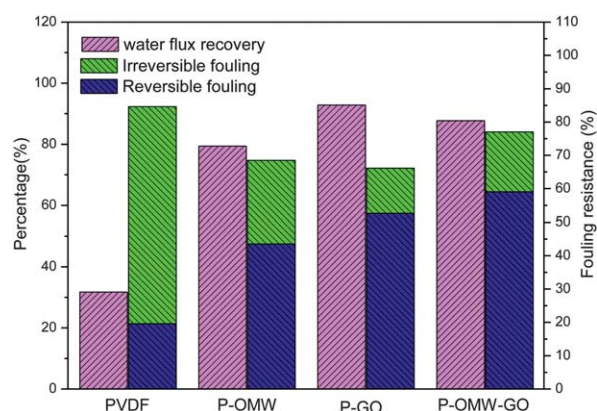


Fig. 9 Water flux recovery and fouling resistance ratio of different membranes.

recovery percentage of the membranes. The flux recovery value of the nascent PVDF membrane was only 29.7%, indicating a poor antifouling property, while it reached about 72.8%, 85.1% and 80.4% by the addition of OMWCNTs, GO and OMWCNTs-GO in the successive three ultrafiltration cycles, respectively. The excellent antifouling performance of the composite membranes may be attributed to the oxygen-containing functional groups in the surface of membranes resulting from the location of the low-dimensional carbon nanomaterials in the surface of the prepared membranes. This leads to a decrease in membrane surface contact angle (Fig. 6) and then improving hydrophilicity of the membrane can reduce membrane fouling to some extent.<sup>65</sup> The higher hydrophilicity could cause formation of a water molecule layer on the PVDF nanocomposite membrane surface and slow the hydrophobic foulants.<sup>52</sup>

To understand more about the fouling phenomenon, resistance parameters such as total ( $R_t$ ), reversible ( $R_r$ ) and irreversible ( $R_{ir}$ ) fouling resistance ratios were calculated from water flux before BSA fouling and after hydraulic cleaning and depicted in Fig. 9. Reversible protein adsorption causes reversible fouling, which could be removed by simple hydraulic cleaning. On the contrary, irreversible fouling results from the strong adsorption of protein molecules on the surface or entrapment of protein molecules in the pores.<sup>66</sup> This implies that the irreversible fouling dominates the total fouling. From Fig. 9, we can see that the  $R_{ir}$  value of the PVDF membrane was 70.9%, which exceeds 75% in total fouling, due to the hydrophobic interactions between the membrane surface and foulant.<sup>44</sup> After modification, the irreversible fouling percentage in the total fouling sharply dropped to 36.4%, 20.5% and 23.4% of P-OMW, P-GO and P-OMW-GO, exhibiting that the antifouling capability of composite membranes was considerably improved. These phenomena could be interpreted as membranes with low-dimensional carbon nanomaterials could induce a denser and more stable hydration layer, which could endow the better antifouling property.<sup>66</sup> Researchers clarified that nanomaterials are being actively explored as antimicrobial components which can be incorporated into membrane structures.<sup>4,67</sup> Considering the above results on flux recovery and the fouling resistance of membranes, we can conclude that low-dimensional carbon nanomaterials are candidates for improving the antifouling properties of membranes.

### Mechanical performance

The tensile strength and elongation-at-break of the membranes are shown in Fig. 10. Both of them tended to rise as the OMWCNTs and GO were added, indicating the reinforcement effect of OMWCNTs and GO on mechanical strength. From Fig. 10, the individual GO or OMWCNTs composite membranes acquire an increase in tensile properties compared with the neat PVDF membranes, however, the tensile strength of P-OMW-GO is similar to that of PVDF membranes. The tensile strength of P-OMW and P-GO show increases of 12.86% and 43.94% compared with that of the PVDF membrane (1.866 MPa), and the ultimate elongation of P-OMW and P-GO was enhanced by 31.50% and 39.24% compared with that of the

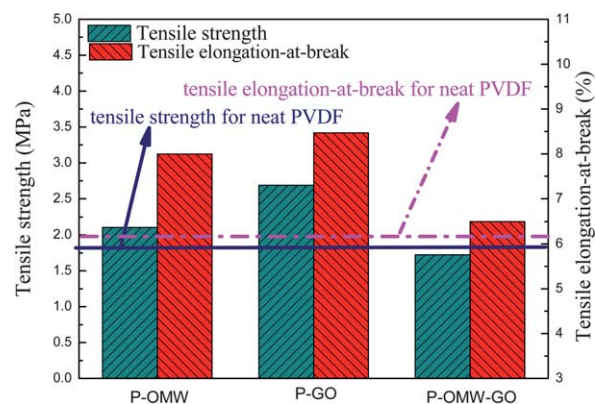


Fig. 10 Tensile strength and elongation-at-break of PVDF, P-OMW, P-GO and P-OMW-GO membranes.

PVDF membrane (6.080%), respectively. This indicates that the composite membranes with oxidized carbon nanomaterials were becoming stronger, but no more brittle than the pure PVDF membrane. Some factors were proposed to explain this phenomenon: the oxidized low-dimensional carbon nanomaterials can act as extensions for the hybrid architectures, which can become entangled with the polymer chain, resulting in a good interaction between OMWCNTs or GO and the PVDF matrix,<sup>68–70</sup> so this further confirms that the oxidized low-dimensional carbon nanomaterials with extremely high specific surface area have a strong interaction with the PVDF matrix and the significantly improved adhesion at interfaces was obtained. Additionally, the mechanical performance improvement of P-GO compared with P-OMW was attributed to the higher specific surface area of GO than OMWCNTs,<sup>71–73</sup> which is an important factor in enhancing the contact area with the PVDF matrix. For another, the slight decrease seen for the tensile strength of P-OMW-GO is due to a bigger mean pore size than PVDF, P-GO and P-OMW, which was caused by the adequately exposed functional groups of GO and OMWCNTs and has an unfavorable influence on the mechanical performance.<sup>74</sup>

From the discussion of the paper, we can conclude that the P-OMW membrane exhibits good rejection and the P-GO membrane shows the potential in water flux recovery and mechanical strength. However, the P-OMW-GO membrane seems to be superior to others in most fields due to the synergistic effect of OMWCNTs and GO and thus deserves to be exploited fully in the future. In addition, after a deep investigation shown in Table 2, it is interesting to contrast the effect of the three-dimensional inorganic particles reported in previous literature and oxidized low-dimensional carbon nanomaterials on the permeation flux, rejection and water flux recovery of PVDF composite membranes. The improved relative percentage of water flux, rejection and water flux recovery for membranes after adding inorganic materials with the minimum concentration was listed in Table 2. It is indicated that the oxidized low-dimensional carbon nanomaterials outperform the other inorganic particles with low specific surface and no oxygen-containing functional groups in the initial pure water flux, rejection and water flux recovery of membranes with the

**Table 2** Contrast of increase in flux, rejection and water flux recovery for membranes after adding the inorganic nanomaterials

Samples	Minimum content of additive (PVDF, g/g)	Relative increased percentage of water flux (%)	Relative increased percentage of rejection (%)	Percentage of water flux recovery (%)	Reference
PVDF-ZrO <sub>2</sub>	50%	4	2.5	—	12
PVDF-LiClO <sub>4</sub>	2.5%	45	—	—	13
PVDF-SiO <sub>2</sub>	1%	25	—	—	15
	1%	33.3	-7.14	60	16
PVDF-Al <sub>2</sub> O <sub>3</sub>	1%	97.7	75	70	14
	1%	120	0.85	27.4	18
PVDF-ZnO	6.7%	20.8	—	91	19
PVDF-Fe <sub>3</sub> O <sub>4</sub>	25%	22.8	6.25	55.2	20
PVDF-TiO <sub>2</sub>	2%	-2	—	—	17
	1%	16.1	5	—	21
PVDF-OMWCNTs	1%	99.33	21.7	72.8	—
PVDF-GO	1%	173.03	17.3	85.1	—
PVDF-OMWCNTs-GO	1%	240.03	14.3	80.4	—

minimum-concentration additive, which illustrates that the introduction of oxidized low-dimensional carbon nanomaterials would be a new pathway for improving the hydrophilicity, pure water flux, rejection, antifouling and mechanical performance of PVDF ultrafiltration membranes.

## Conclusions

The PVDF-based ultrafiltration membranes have been prepared from a complex comprising PVDF and oxidized low-dimensional carbon nanomaterials by the phase inversion method. Taking into account all the evidence outlined, we may reasonably reach the conclusions as follows:

(1) The composite membranes containing OMWCNTs and GO have the bigger mean pore size and higher surface roughness than neat PVDF membranes, which undoubtedly played a positive role in promoting membrane permeability.

(2) The effect of OMWCNTs and GO on membrane hydrophilicity was striking and the contact angle of membranes decreased from 78.536° (pure PVDF) to 66.845° (PVDF-OMWCNTs), 66.4° (PVDF-GO) and 48.582° (PVDF-OMWCNTs-GO), which was attributed mainly to the presence of oxygen-containing functional groups on oxidized low-dimensional carbon nanomaterials surfaces.

(3) The pure water flux of the PVDF-OMWCNTs, PVDF-GO and PVDF-OMWCNTs-GO membranes was increased by 99.33%, 173.03% and 240.03% and the BSA rejection was enhanced by 21.71%, 17.23% and 14.29%, respectively, compared with those of pure PVDF membranes, surpassing those of reported membranes with three-dimensional inorganic particles. The PVDF-GO membranes performed better in water flux, but worse in BSA rejection than PVDF-OMWCNTs membranes, owing to the big mean pore size of P-GO caused by the adequately exposed functional groups and high specific surface of GO.

(4) The tensile strength and elongation-at-break of membranes containing OMWCNTs and GO were improved by 12.86%, 43.94% and 31.50%, 39.24%, respectively. But there was a slight decrease for the mechanical performance of PVDF-OMWCNTs-GO membranes due to the negative effect of a big

pore size caused by the synergistic effect of OMWCNTs and GO, which was beneficial to the hydrophilicity and pure water flux of membranes.

(5) From the multi-cycle operations, the flux recovery reached about 72.8%, 85.1% and 80.4% by the addition of OMWCNTs, GO and OMWCNTs-GO, while it was only 29.7% for the raw membrane, indicating an impressive prospect for the antifouling performance and the recycling of composite membranes.

In view of the conclusion discussed above, the PVDF composite membranes tailored by oxidized low-dimensional carbon nanomaterials hold a great potential for being robust ultrafiltration membranes and need to be further exploited fully.

## Acknowledgements

The work was funded by the National Natural Science Foundation of China (11175130), the Natural Science Foundation of Tianjin, China (10JCYBJC02300), the China Postdoctoral Science Foundation (2012M520578, 20100481092) and the Jiangsu Planned Projects for Postdoctoral Research Funds (1002031C).

## Notes and references

- Z. Ademovic, D. Klee, P. Kingshott, R. Kaufmann and H. Hocker, *Biomol. Eng.*, 2002, **19**, 177–182.
- N. Wang, X. Wang, B. Ding, J. Yu and G. Sun, *J. Mater. Chem.*, 2012, **22**, 1445–1452.
- M. A. Shannon, P. W. Bohn, M. Elimelech, J. G. Georgiadis, B. J. Marinas and A. M. Mayes, *Nature*, 2008, **452**, 301–310.
- J. Mansouri, S. Harisson and V. Chen, *J. Mater. Chem.*, 2010, **20**, 4567–4586.
- I. S. Chang, C. M. Chung and S. H. Han, *Desalination*, 2001, **133**, 225–232.
- H. Ma, C. Burger, B. S. Hsiao and B. Chu, *J. Mater. Chem.*, 2011, **21**, 7507–7510.
- Q. Yang, N. Adrus, F. Tomicki and M. Ulbricht, *J. Mater. Chem.*, 2011, **21**, 2783.

- 8 M. Tao, F. Liu and L. Xue, *J. Mater. Chem.*, 2012, **22**, 9131–9137.
- 9 Y. Xuanxuan, Z. Bowu, L. Zhongying, D. Bo, Y. Ming, L. Linfan, J. Haiqing and L. Jingye, *J. Mater. Chem.*, 2011, **21**, 11908–11915.
- 10 P. Wang, K. L. Tan, E. T. Kang and K. G. Neoh, *J. Mater. Chem.*, 2001, **11**, 783–789.
- 11 X. Zhihong, L. Lei, W. Fawen, T. Shujuan and Z. Zhibing, *J. Membr. Sci.*, 2005, **255**, 125–131.
- 12 A. Bottino, G. Capannelli and A. Comite, *Desalination*, 2002, **146**, 35–40.
- 13 D. J. Lin, C. L. Chang, F. M. Huang and L. P. Cheng, *Polymer*, 2003, **44**, 413–422.
- 14 F. Liu, M. R. M. Abed and K. Li, *J. Membr. Sci.*, 2011, **366**, 97–103.
- 15 A. Cui, Z. Liu, C. Xiao and Y. Zhang, *J. Membr. Sci.*, 2010, **360**, 259–264.
- 16 L. Y. Yu, Z. L. Xu, H. M. Shen and H. Yang, *J. Membr. Sci.*, 2009, **337**, 257–265.
- 17 S. J. Oh, N. Kim and Y. T. Lee, *J. Membr. Sci.*, 2009, **345**, 13–20.
- 18 L. Yan, Y. S. Li, C. B. Xiang and S. Xianda, *J. Membr. Sci.*, 2006, **276**, 162–167.
- 19 S. Liang, K. Xiao, Y. Mo and X. Huang, *J. Membr. Sci.*, 2012, **394**, 184–192.
- 20 Z.-Q. Huang, F. Zheng, Z. Zhang, H.-T. Xu and K.-M. Zhou, *Desalination*, 2012, **292**, 64–72.
- 21 Y. Wei, H.-Q. Chu, B.-Z. Dong, X. Li, S.-J. Xia and Z.-M. Qiang, *Desalination*, 2011, **272**, 90–97.
- 22 J. K. Holt, H. G. Park, Y. M. Wang, M. Stadermann, A. B. Artyukhin, C. P. Grigoropoulos, A. Noy and O. Bakajin, *Science*, 2006, **312**, 1034–1037.
- 23 B. J. Hinds, N. Chopra, T. Rantell, R. Andrews, V. Gavalas and L. G. Bachas, *Science*, 2004, **303**, 62–65.
- 24 H. Brody, *Nature*, 2012, **483**, S29.
- 25 J. A. Rogers, M. G. Lagally and R. G. Nuzzo, *Nature*, 2011, **477**, 45–53.
- 26 L. Y. Jiao, L. Zhang, X. R. Wang, G. Diankov and H. J. Dai, *Nature*, 2009, **458**, 877–880.
- 27 K. Sangil, J. R. Jinschek, H. Chen, D. S. Sholl and E. Marand, *Nano Lett.*, 2007, **7**, 2806–2811.
- 28 P. Wang, J. Ma, Z. Wang, F. Shi and Q. Liu, *Langmuir*, 2012, **28**, 4776–4786.
- 29 S. Majeed, D. Fierro, K. Buhr, J. Wind, B. Du, A. Boschetti-de-Fierro and V. Abetz, *J. Membr. Sci.*, 2012, **403–404**, 101–109.
- 30 E.-S. Kim, G. Hwang, M. G. El-Din and Y. Liu, *J. Membr. Sci.*, 2012, **394**, 37–48.
- 31 J. Heo, J. R. V. Flora, N. Her, Y.-G. Park, J. Cho, A. Son and Y. Yoon, *Sep. Purif. Technol.*, 2012, **90**, 39–52.
- 32 E. Celik, H. Park and H. Choi, *Water Res.*, 2011, **45**, 274–282.
- 33 P. Gunawan, C. Guan, X. Song, Q. Zhang, S. S. J. Leong, C. Tang, Y. Chen, M. B. Chan-Park, M. W. Chang, K. Wang and R. Xu, *ACS Nano*, 2011, **5**, 10033–10040.
- 34 H. Q. Wu, B. B. Tang and P. Y. Wu, *J. Membr. Sci.*, 2010, **362**, 374–383.
- 35 S. Qiu, L. Wu, X. Pan, L. Zhang, H. Chen and C. Gao, *J. Membr. Sci.*, 2009, **342**, 165–172.
- 36 A. Rahimpour, M. Jahanshahi, S. Khalili, A. Mollahosseini, A. Zirepour and B. Rajaeian, *Desalination*, 2012, **286**, 99–107.
- 37 C. Jin, J. Liu, L. Li and Y. Bai, *J. Membr. Sci.*, 2009, **341**, 233–237.
- 38 P. Wang, J. Ma, Z. Wang, F. Shi and Q. Liu, *Langmuir*, 2012, **28**, 4776–4786.
- 39 K. A. Wepasnick, B. A. Smith, K. E. Schrote, H. K. Wilson, S. R. Diegelmann and D. H. Fairbrother, *Carbon*, 2011, **49**, 24–36.
- 40 S.-Y. Yang, W.-N. Lin, Y.-L. Huang, H.-W. Tien, J.-Y. Wang, C.-C. M. Ma, S.-M. Li and Y.-S. Wang, *Carbon*, 2011, **49**, 793–803.
- 41 J.-F. Li, Z.-L. Xu and H. Yang, *Polym. Adv. Technol.*, 2008, **19**, 251–257.
- 42 C. S. Feng, B. L. Shi, G. M. Li and Y. L. Wu, *J. Membr. Sci.*, 2004, **237**, 15–24.
- 43 C. Agarwal, A. K. Pandey, S. Das, M. K. Sharma, D. Pattyn, P. Ares and A. Goswami, *J. Membr. Sci.*, 2012, **415**, 608–615.
- 44 D.-G. Kim, H. Kang, S. Han and J.-C. Lee, *J. Mater. Chem.*, 2012, **22**, 8654.
- 45 S. Yang, J. Li, D. Shao, J. Hu and X. Wang, *J. Hazard. Mater.*, 2009, **166**, 109–116.
- 46 N. L. An, H. Z. Liu, Y. C. Ding, M. Zhang and Y. P. Tang, *Appl. Surf. Sci.*, 2011, **257**, 3831–3835.
- 47 A. Bottino, G. Camera-Rodab, G. Capannellic and S. Munaria, *J. Membr. Sci.*, 1991, **57**, 1–20.
- 48 M. Tao, F. Liu and L. Xue, *J. Mater. Chem.*, 2012, **22**, 9131.
- 49 V. Vatanpour, S. S. Madaeni, R. Moradian, S. Zinadini and B. Astinchap, *J. Membr. Sci.*, 2011, **375**, 284–294.
- 50 R. N. Wenzel, *Ind. Eng. Chem.*, 1936, **28**, 988–994.
- 51 V. Vatanpour, S. S. Madaeni, R. Moradian, S. Zinadini and B. Astinchap, *Sep. Purif. Technol.*, 2012, **90**, 69–82.
- 52 V. Vatanpour, S. S. Madaeni, L. Rajabi, S. Zinadini and A. A. Derakhshan, *J. Membr. Sci.*, 2012, **401**, 132–143.
- 53 P. van der Marel, A. Zwijnenburg, A. Kemperman, M. Wessling, H. Temmink and W. van der Meer, *J. Membr. Sci.*, 2010, **348**, 66–74.
- 54 L. Palacio, J. I. Calvo, P. Pradanos, A. Hernandez, P. Vaisanen and M. Nystrom, *J. Membr. Sci.*, 1999, **152**, 189–201.
- 55 J.-H. Choi, J. Jegal and W.-N. Kim, *J. Membr. Sci.*, 2006, **284**, 406–415.
- 56 M. K. Shin, B. Lee, S. H. Kim, J. A. Lee, G. M. Spinks, S. Gambhir, G. G. Wallace, M. E. Kozlov, R. H. Baughman and S. J. Kim, *Nat. Commun.*, 2012, **3**, 650.
- 57 S. M. Luna, S. S. Silva, M. E. Gomes, J. F. Mano and R. L. Reis, *J. Biomater. Appl.*, 2011, **26**, 101–116.
- 58 Y. N. Yang, P. Wang and Q. Z. Zheng, *J. Polym. Sci., Part B: Polym. Phys.*, 2006, **44**, 879–887.
- 59 J. Meng, L. Song, H. Xu, H. Kong, C. Wang, X. Guo and S. Xie, *Nanomed.: Nanotechnol., Biol. Med.*, 2005, **1**, 136–142.
- 60 M. Hashino, K. Hiram, T. Ishigami, Y. Ohmukai, T. Maruyama, N. Kubota and H. Matsuyama, *J. Membr. Sci.*, 2011, **384**, 157–165.
- 61 K.-J. Hwang and P.-Y. Sz, *J. Membr. Sci.*, 2011, **378**, 272–279.
- 62 L. Wang, Y.-I. Su, L. Zheng, W. Chen and Z. Jiang, *J. Membr. Sci.*, 2009, **340**, 164–170.

- 63 D. Rana and T. Matsuura, *Chem. Rev.*, 2010, **110**, 2448–2471.
- 64 G. B. Sigal, M. Mrksich and G. M. Whitesides, *J. Am. Chem. Soc.*, 1998, **120**, 3464–3473.
- 65 X. L. Li, L. P. Zhu, B. K. Zhu and Y. Y. Xu, *Sep. Purif. Technol.*, 2011, **83**, 66–73.
- 66 J. Peng, Y. Su, Q. Shi, W. Chen and Z. Jiang, *Bioresour. Technol.*, 2011, **102**, 2289–2295.
- 67 Q. Li, S. Mahendra, D. Y. Lyon, L. Brunet, M. V. Liga, D. Li and P. J. J. Alvarez, *Water Res.*, 2008, **42**, 4591–4602.
- 68 C. Lin and D. D. L. Chung, *Carbon*, 2009, **47**, 295–305.
- 69 A. Yu, P. Ramesh, M. E. Itkis, E. Bekyarova and R. C. Haddon, *J. Phys. Chem. C*, 2007, **111**, 7565–7569.
- 70 M. T. Hung, O. Choi, Y. S. Ju and H. T. Hahn, *Appl. Phys. Lett.*, 2006, **89**, 023117(1–3).
- 71 J. Li and J.-K. Kim, *Compos. Sci. Technol.*, 2007, **67**, 2114–2120.
- 72 X. M. Chen, J. W. Shen and W. Y. Huang, *J. Mater. Sci. Lett.*, 2002, **21**, 213–214.
- 73 W. G. Weng, G. H. Chen, D. J. Wu and W. L. Yan, *Compos. Interfaces*, 2004, **11**, 131–143.
- 74 N. Scharnagl and H. Buschatz, *Desalination*, 2001, **139**, 191–198.